Effects of front width on acoustic ducting by a continuous curved front over a sloping bottom

Brendan J. DeCourcy, Ying-Tsong Lin, and William L. Siegmann

ARTICLES YOU MAY BE INTERESTED IN

Effects of front width on acoustic ducting by a continuous curved front over a sloping bottom

Brendan J. DeCourcy,[1,a] Ying-Tsong Lin,[1] and William L. Siegmann[2]

[1]*Applied Ocean Physics and Engineering, Woods Hole Oceanographic Institution, Woods Hole, Massachusetts 02543, USA*
[2]*Department of Mathematical Sciences, Rensselaer Polytechnic Institute, Troy, New York 12180, USA*

The behavior of sound near an ocean front in a region with wedge bathymetry is examined. The front is parameterized as a zone of variation with inshore and offshore boundaries parallel to a straight coastline. The importance of frontal width and frontal sound speed on the ducting of acoustic energy is examined. Previous analytical studies of sound propagation and parameter sensitivity in an idealized wedge environment use an unphysical but convenient single interface front representation, which is here replaced by a continuous sound speed profile. The continuous profile selected is convenient for analytical investigation, but encourages the use of asymptotic approximation methods which are also described. The analytical solution method is outlined, and numerical results are produced with an emphasis on comparing to the single interface front. These comparisons are made to highlight the strengths and weaknesses of the idealized model for capturing the horizontal ducting effects. © 2019 Acoustical Society of America.
https://doi.org/10.1121/1.5125426

I. INTRODUCTION

Over the sloping bathymetry of a coastal shelf, sound speed fronts occur due to temperature, density, and salinity gradients.[1–5] In a shelf-break front environment, the ocean can be generally divided into three regions characterized by sound speed behavior: inshore, offshore, and frontal. Within the front, the sound speed gradient in range is larger when compared to the more slowly varying inshore and offshore regions. This kind of ocean feature can influence acoustic propagation through along-shore ducting and refraction of acoustic energy by the front. Using mathematical models of a curved coastal front, the importance of front width can be determined, with prior analyses of a similar environment from Lin and Lynch providing a baseline for comparisons.[6–8]

To examine the ducting effects of front width over a sloping bottom, the idealized front of Lin and Lynch is considered.[6] This model describes the front as an instantaneous change between isospeed inshore and offshore regions. While convenient for analytic calculations, the effects of a more physical continuously varying ocean are lost. This paper will introduce a range dependent continuous inverse-square wavenumber profile, which has the advantages of representing a continuously varying sound speed front in a mathematically convenient form, as well as having some established applications in ocean acoustics literature.[9,10] The method of normal modes is applied, with the Wentzel-Kramers-Brillouin-Jeffreys (WKBJ) approximation introduced for the front region to facilitate numerical calculation of radial modes. Horizontal wavenumber eigenvalues, radial mode eigenfunctions, and transmission loss fields are calculated for various front widths to illustrate front width influence on acoustic pressure. While this paper seeks to address one unphysical aspect of the idealized wedge model, other properties such as bottom attenuation and variability in the front structure have been examined by other authors.[11–14]

II. MODEL DEVELOPMENT AND ANALYTICAL SOLUTION

The solution method presented here will follow closely those methods outlined by Frisk[15] and Lin and Lynch[6] for acoustic pressure in a wedge with an impenetrable bottom and a pressure release surface. This formulation will introduce a continuously varying front region of constant curvature with an inshore point source located at (r_0, θ_0, y_0) in cylindrical coordinates as illustrated in Fig. 1. Spatial coordinates in the wedge are y which is coincident with the shoreline, θ measuring angular displacement from the surface at $\theta = 0$ and increasing towards the bottom at $\theta = \alpha$, and r which is distance from the shoreline measured perpendicular to the shore. The front is centered at $r = r_I$ with a width of s, and the sound speed inshore and offshore are given by the constants c_1 and c_2 respectively, with a continuous $c_F(r)$ satisfying $c(r_j) = c_j$ at the inshore and offshore interfaces r_1 and r_2. Acoustic pressure is given by the Helmholtz equation

$$\left[\nabla^2 + k^2(r)\right] P(r, \theta, y) = -4\pi \frac{\partial(r - r_0)}{r} \partial(\theta - \theta_0)\delta(y),$$

(1)

where $k(r)$ is the range-dependent wavenumber, the time evolution of the single frequency point source has been

---

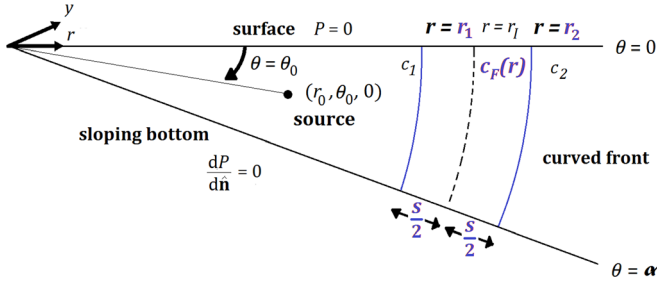a)Electronic mail: bdecourcy@whoi.edu

FIG. 1. (Color online) Model geometry for the shelf-slope wedge with continuous sound speed front. Model parameters are: front location r_I, front width s, bottom slope angle α, source frequency f, inshore/offshore sound speeds c_1/c_2. Boundary conditions are pressure release at the surface $\theta = 0$ and reflection at the bottom $\theta = \alpha$.
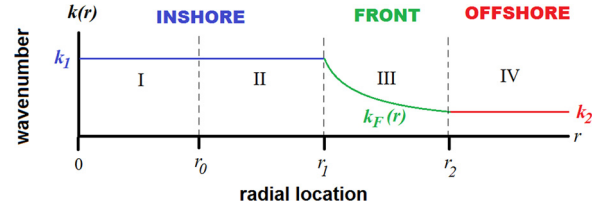

FIG. 2. (Color online) Illustration of four radially defined ocean regions of physical importance in the model. The inshore region is comprised of I and II, which in turn lie on either side of the radial location of the inshore point source at $r = r_0$. The front region is denoted by III, while the offshore region is IV.

accounted for by factoring out $e^{-i\omega t}$, the source frequency given by $\omega = 2\pi f$, $p(r, \theta, y, t) = P(r, \theta, y)e^{-i\omega t}$, and with a unit source strength of 1, with the appropriate implied units of energy per length squared (J/m^2). Boundary and interface conditions on P are $P(r, 0, y) = 0$ (pressure release), $\partial P/\partial\theta|_{\theta=\alpha} = 0$ (reflecting bottom), $P(0, \theta, y) < \infty$ (pressure is finite at the wedge apex), the Sommerfeld radiation condition as $r \to \infty$, and impedance interface conditions at $r = r_j$.

The along-shore spatial coordinate y can be converted to and from the horizontal wavenumber spectrum k_y through the Fourier transform pair

$$P(r, \theta, y) = \frac{1}{2\pi} \int_{-\infty}^{\infty} G(r, \theta, k_y)e^{ik_y y}dk_y, \tag{2}$$

$$G(r, \theta, k_y) = \int_{-\infty}^{\infty} P(r, \theta, y)e^{-ik_y y}dy. \tag{3}$$

The function G solves the radial mode equation

$$\frac{1}{r}\frac{\partial}{\partial r}\left(r\frac{\partial G}{\partial r}\right) + \frac{1}{r^2}\frac{\partial^2 G}{\partial\theta^2} + (k^2 - k_y^2)G$$
$$= -4\pi\frac{\partial(r - r_0)}{r}\partial(\theta - \theta_0), \tag{4}$$

and can be represented by a sum of separated eigenfunctions

$$G = \sum_n \Phi_n(\theta_0)\Phi_n(\theta)A_n(r, k_y). \tag{5}$$

A set of orthonormal angular eigenfunctions $\Phi_n(\theta) = \sqrt{(2/\alpha)}\sin(\eta_n\theta)$ can be derived, where $\eta_n = (\pi/\alpha)(n - 1/2)$

is a separation constant as well as the dimensionless angular wavenumber. With this definition for the angular eigenfunctions the radial mode equation takes the form of a Bessel equation for the inshore and offshore regions, for which the wavenumber is the constant value $k_j = 2\pi f/c_j$ with $j = 1$ or 2 denoting inshore or offshore, respectively.[6,15] Due to the chosen coordinate system and model geometry, G is completely separable as shown in Eq. (5). Range-dependent perturbations to the model that would break the separability of G will require a mode coupling treatment.[16]

Within the front region, the square of the wavenumber will be represented by an inverse square wavenumber profile $k_F(r) = \sqrt{a^2 + b^2/r^2}$ as shown in Fig. 2, which allows the radial mode equation to remain a Bessel type equation,

$$\frac{1}{r}\frac{d}{dr}\left(r\frac{dA_n}{dr}\right) + \left((a^2 - k_y^2) - \frac{(\eta_n^2 - b^2)}{r^2}\right)A_n$$
$$= -4\pi\frac{\delta(r - r_0)}{r}. \tag{6}$$

The constants a and b are chosen such that $k(r_1) = k_1$ and $k(r_2) = k_2$. The radial mode function A_n is determined by matching two solutions of the radial mode equation found with the method of variation of parameters, each solving one of the boundary conditions (at $r = 0$, and at $r = r_1$) on either side of the point source at $r = r_0$,[6,15,17] and is expressed as a linear combination of Bessel type functions as

$$A_n(r, k_y) = \frac{i2\pi^2}{1 - R_n}J_{\eta_n}(k_{r1}r_0)B_n(r, k_y), \tag{7}$$

where $k_{r1} = \sqrt{k_1^2 - k_y^2}$, R_n acts like a reflection coefficient related to energy that returns to the inshore region $r < r_1$ after being refracted back by the front, and J_n is the Bessel function of the first kind. The function B_n is

$$B_n(r, k_y) = \begin{cases} \dfrac{1}{2}\dfrac{J_{\eta_n}(k_{r1}r)}{J_{\eta_n}(k_{r1}r_0)}\left[H_{\eta_n}^{(1)}(k_{r1}r_0) + R_nH_{\eta_n}^{(2)}(k_{r1}r_0)\right], & 0 \leq r < r_0, \\[2ex] \dfrac{1}{2}\left[H_{\eta_n}^{(1)}(k_{r1}r) + R_nH_{\eta_n}^{(2)}(k_{r1}r)\right], & r_0 < r \leq r_1, \\[2ex] d_{1n}H_{-i\nu_n}^{(1)}(k_{rF}r) + d_{2n}H_{-i\nu_n}^{(2)}(k_{rF}r), & r_1 \leq r \leq r_2, \\[2ex] T_nH_{\eta_n}^{(1)}(k_{r2}r), & r_2 \leq r, \end{cases} \tag{8}$$

where $k_{r2} = \sqrt{k_2^2 - k_y^2}$, $\nu_n = \sqrt{b^2 - \eta_n^2}$, $k_{rF} = \sqrt{a^2 - k_y^2}$, and $H_{\eta_n}^{(1,2)}$ are Hankel functions of the first and second kind. Figure 2 illustrates the division of r into four regions I, II, III, and IV relative to the r locations 0, r_0, r_1, and r_2, with I and II representing the inshore region, III the front, and IV offshore. The quantity R_n can be derived by satisfying the conditions of continuity for the radial mode function and its derivative at r_1 and r_2, and the condition of finiteness at $r = 0$. It is expressed as

$$R_n = -\frac{\Delta_{11}\mathcal{E}_1 - \Delta_{12}\mathcal{E}_2}{\Delta_{21}\mathcal{E}_1 - \Delta_{12}\mathcal{E}_2}\mathcal{F}D, \qquad (9)$$

where

$$\Delta_{pq} = \frac{k_{rq}\dfrac{H_{\eta_n}^{(p)\prime}(k_{rq}r_q)}{H_{\eta_n}^{(p)}(k_{rq}r_q)} - k_{rF}\dfrac{H_{-i\nu_n}^{(1)\prime}(k_{rF}r_q)}{H_{-i\nu_n}^{(1)}(k_{rF}r_q)}}{k_{rq}\dfrac{H_{\eta_n}^{(p)\prime}(k_{rq}r_q)}{H_{\eta_n}^{(p)}(k_{rq}r_q)} - k_{rF}\dfrac{H_{-i\nu_n}^{(2)\prime}(k_{rF}r_q)}{H_{-i\nu_n}^{(2)}(k_{rF}r_q)}}, \qquad (10)$$

$$\mathcal{F} = \frac{k_{r1}\dfrac{H_{\eta_n}^{(1)\prime}(k_{r1}r_1)}{H_{\eta_n}^{(1)}(k_{r1}r_1)} - k_{rF}\dfrac{H_{-i\nu_n}^{(2)\prime}(k_{rF}r_1)}{H_{-i\nu_n}^{(2)}(k_{rF}r_1)}}{k_{r1}\dfrac{H_{\eta_n}^{(2)\prime}(k_{r1}r_1)}{H_{\eta_n}^{(2)}(k_{r1}r_1)} - k_{rF}\dfrac{H_{-i\nu_n}^{(2)\prime}(k_{rF}r_1)}{H_{-i\nu_n}^{(2)}(k_{rF}r_1)}}. \qquad (11)$$

$$\mathcal{E}_q = \frac{H_{-i\nu_n}^{(1)}(k_{rF}r_q)}{H_{-i\nu_n}^{(2)}(k_{rF}r_q)}, \quad D = \frac{H_{\eta_n}^{(1)}(k_{r1}r_1)}{H_{\eta_n}^{(2)}(k_{r1}r_1)}. \qquad (12)$$

The coefficients d_{1n}, d_{2n}, and T_n can be found simultaneously with R_n by satisfying the continuity conditions on the radial mode function and its derivative.

The pressure P can now be expressed as

$$P(r,\theta,y) = i\frac{2\pi}{\alpha}\sum_n \sin(\eta_n\theta_0)\sin(\eta_n\theta)$$
$$\times \int_{-\infty}^{\infty}\frac{J_{\eta_n}(k_{r1}r_0)B_n(r,k_y)e^{ik_y y}}{1-R_n}dk_y, \qquad (13)$$

after substituting Eqs. (5), (7), and (8) into Eq. (2). The integral in Eq. (13) can be approximated by complex integration using residue theory. First, the existence of the square roots in B_n introduce branch cuts in the k_y plane emanating from the points $\pm k_1$, $\pm k_2$, and $\pm a$. The Pekeris branch cut will be used for these, which will expose leaky mode eigenvalues in the first quadrant of the k_y plane.[18] The Hankel functions have a singularity where the argument is zero, occurring at the branch points $\pm k_1$, $\pm k_2$, and $\pm a$, which will be excluded from the interior of the closed integration path to be chosen in the k_y plane. There will be singularities in the integrand where $R_n = 1$, which are also the locations of the eigenvalues in the k_y plane denoted $k_{y,nm}$, where m represents the m-th radial mode eigenvalue associated with angular mode n.

A closed integration path illustrated in Fig. 3 and as described in Lin and Lynch is used, which includes a segment along the real k_y axis that avoids branch points,
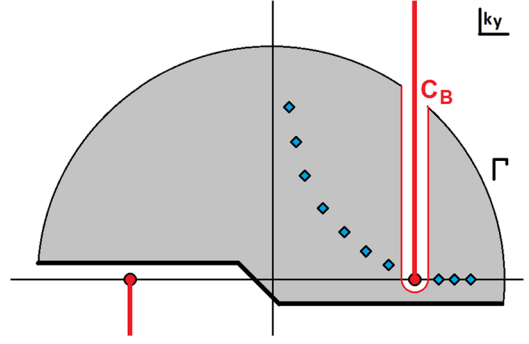

FIG. 3. (Color online) The Pekeris branch cut, isolating the integration path around the branch line C_B, and exposing the leaky mode eigenvalues (blue diamonds above the horizontal real axis).

integration paths that run along either side of the branch lines in the first quadrant of the k_y plane, and a path that approaches infinity in the upper half k_y plane.[6] The integral along the last integration path vanishes, while the branch line integrals can be ignored if only the far field is of interest.[18,19] For a closed path Γ as described above, the far-field approximation and the residue theorem[20] together state that $\int_{-\infty}^{\infty} \approx \int_{\Gamma} = 2\pi i\sum(\text{residues})$,

$$P(r,\theta,y) \approx -\frac{4\pi^2}{\alpha}\sum_n \sin(\eta_n\theta_0)\sin(\eta_n\theta)\sum_m e^{ik_{y,nm}y}$$
$$\times \text{Res}\left(\frac{J_{\eta_n}(k_{r1}r_0)B_n(r,k_y)e^{ik_y y}}{1-R_n}, k_{y,nm}\right), \qquad (14)$$

where $\text{Res}(F(z), z_m)$ is the residue of F at z_m, and is defined by $(1/2\pi i)\int_{C_m}F(z)dz = \text{Res}(F(z), z_m)$, for a closed contour C_m which contains only z_m and no other singularities.[20] Because Hankel functions only have singularities[21] in the k_y plane where $k_y = \pm k_1$, $\pm k_2$, $\pm a$, and as it is unlikely that an eigenvalue will coincide with these values, a path C_m can be defined in a neighborhood of any $k_{y,nm}$ that will not contain any singularities arising from the Hankel functions. There may be locations in the k_y plane where d_{1n}, d_{2n}, T_n, or R_n have singularities. Again, these are not expected to coincide with $k_{y,nm}$ in which case there will be a valid contour C_m to calculate the residue.

The residue in Eq. (14) is calculated under the assumption that the $k_{y,nm}$ are simple poles. A pole at $k_{y,nm}$ will have multiplicity higher than 1 if $(\partial/\partial k_y)(1 - R_n)_{k_y=k_{y,nm}} = 0$, in which case the complex integration requires more care.[22,23] Due to the complexity of the dispersion relation for this model, its derivative can be tested numerically for each eigenvalue to determine if its multiplicity is higher than 1. For eigenvalues tested and presented in this paper, none have multiplicity higher than 1, so calculations will proceed with this in mind. For simple poles, Eq. (14) can be approximated as

$$P(r,\theta,y) \approx \frac{4\pi^2}{\alpha}\sum_{n,m}\sin(\eta_n\theta_0)\sin(\eta_n\theta)J_{\eta_n}(k_{r1,nm}r_0)$$
$$\times \left[\frac{dR_n}{dk_y}\bigg|_{k_y=k_{y,nm}}\right]^{-1}\Psi_n(r,k_{y,nm})e^{ik_{y,nm}y}, \qquad (15)$$

with

J. Acoust. Soc. Am. **146** (3), September 2019

DeCourcy *et al.*   1925

$$\Psi_n(r, k_{y,nm}) = \begin{cases} J_{\eta_n}(k_{r1,nm}r), & 0 \le r \le r_1, \\ d_{1n}H^{(1)}_{-i\nu_n}(k_{rF,nm}r) + d_{2n}H^{(2)}_{-i\nu_n}(k_{rF,nm}r), & r_1 \le r \le r_2, \\ T_nH^{(1)}_{\eta_n}(k_{r2,nm}r), & r_2 \le r. \end{cases} \qquad (16)$$

III. WKBJ APPROXIMATION OF THE FRONT REGION

To aid in numerical computations involving radial behavior in the front, the radial mode equation within the front will be approximated using the WKBJ method, which will yield approximated radial mode functions and an approximated dispersion relation. The first step will be to transform the radial mode equation into a more convenient form by introducing the function $\beta(\tau) = r^{1/2}\Psi(r)$, where $\tau = r_I^{-1}r$. This leads to the equation

$$\delta^2\beta''(\tau) - h(\tau)\beta(\tau) = 0, \qquad (17)$$

where

$$h(\tau) = \left(\frac{1}{\tau_t^2} - \frac{1}{\tau^2}\right), \qquad (18)$$

and $\delta = (\nu^2 + 1/4)^{-1/2}$, and $\tau_t = (q_F r_I \delta)^{-1}$. The term $q_F^2 = -k_{rF}^2$ has been introduced, because for lower radial mode numbers which are associated with the trapped modes, $a^2 < k_y^2$ for real k_y. For k_y within the WG and TR regions, $\tau_t \sim 1$, and will grow as radial mode number increases.

The function $h(\tau)$ has a zero at $\tau = \tau_t$, so τ_t is a turning point of Eq. (17) where the behavior of $\beta(\tau)$ transitions between exponential and oscillatory. This information can be used to classify radial mode behavior and types, by using the oscillatory or exponential characteristics of a mode to determine if it is trapped or leaky. Introducing the notation $\kappa_r(r) = \sqrt{k^2(r) - k_y^2 - (\eta_n^2/r^2)}$ to represent the radial wavenumber as the square root of the square of the wavenumber in the water minus the squares of the horizontal wavenumber k_y and the scaled azimuthal wavenumber η_n/r, the function $h(\tau)$ can be expressed as

$$h(\tau) = -r_I^2\delta^2\left(\kappa_r^2(r) - \frac{1}{4r^2}\right). \qquad (19)$$

Therefore, the turning point in r, given by r_t occurs when $\kappa_r(r_t) = 1/(2r_t)$, for some $r_1 < r_t < r_2$. Solving for r_t gives $r_t = q_F^{-1}\sqrt{\nu_n^2 - 1} \sim \nu_n/q_F$, which is the location at which $\kappa_r(r) = 0$. Because r_t is dependent on k_y, for a given eigenvalue $k_{y,nm}$, the radial mode shape will differ as k_y changes.

Figure 4 illustrates the expected behavior of the radial mode functions by indicating oscillatory or exponential behavior in the $(\eta^2/r^2, \mathrm{Re}(k_y)^2)$ plane, with the zeros of $\kappa_r(r)$ shown as thick solid lines. Three clear mode types appear in the illustration: whispering gallery (WG) modes are trapped modes with purely exponential decay offshore for real k_y, leaky modes with purely oscillatory behavior offshore, and between the two in the k_y spectrum are transition (TR) modes which are not trapped, but which transmit less energy offshore due to the range-dependent nature of the radial wavenumber. This behavior for TR modes is seen in the mixed exponential behavior between the offshore interface of the front at r_2, and an offshore turning point at $\kappa_{r2}(r) = 0$, before they transition to purely oscillatory behavior beyond the turning point. The real k_y spectrum is therefore divided into three regions, with WG modes occurring when $k_2 < \mathrm{Re}(k_y) < k_1^*$, TR modes occurring when $k_2^* < \mathrm{Re}(k_y) < k_2$, and leaky modes occurring when $0 < \mathrm{Re}(k_y) < k_2^*$. The quantity k_j^* denotes locations at which
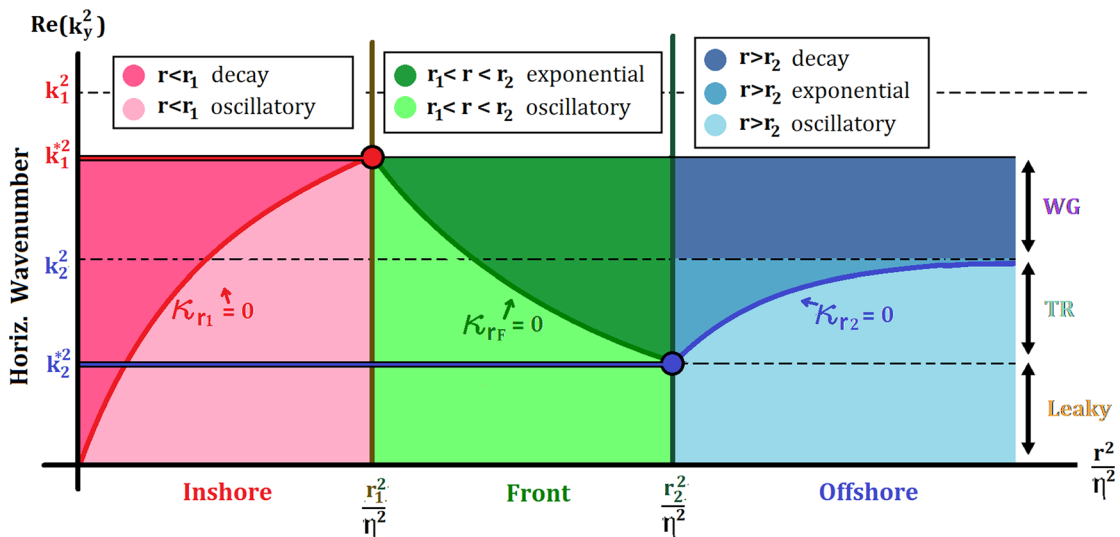
FIG. 4. (Color online) Diagram of the general mode behavior in r dependent on horizontal wavenumber k_y in the $(\eta_n^2/r^2, \mathrm{Re}(k_y^2))$ plane. Curves for $\kappa_r(r) = 0$ are labeled in the figure, with regions above the curves exhibiting exponential behavior and regions below exhibiting oscillatory behavior. Three mode types are identified based on the exponential/oscillatory distinctions: whispering gallery (WG), transition (TR), and leaky.

the radial wavenumber will have zero real part at r_1 or r_2, and is defined $k_j^* = \sqrt{k_j^2 - (\eta_n^2/r^2)}$.

For complex k_y, $\mathrm{Re}(\tau_t) > 0$, and due to the fact that $\mathrm{Re}(k_y) \gg \mathrm{Im}(k_y)$ in the WG and TR regions (to be shown in Sec. IV, and as seen in Refs. 6 and 7) as well as for a considerable number of leaky modes, the introduction of a nonzero imaginary component of k_y will serve to slightly perturb the behavior of the WG mode approximations that assume $\mathrm{Im}(k_y) = 0$. For this reason, classification of modes henceforth will be based solely on the real component of k_y, and the imaginary component of r_t will not be considered.

For small δ in Eq. (17), the uniformly valid WKBJ approximation is[24]

$$\beta(\tau) \sim \delta^{-1/6} \left(\frac{f(\tau)}{h(\tau)} \right)^{1/4} \left[a_0 \mathrm{Ai}\left(\delta^{-2/3} f(\tau) \right) + b_0 \mathrm{Bi}\left(\delta^{-2/3} f(\tau) \right) \right], \tag{20}$$

where

$$f(\tau) = \begin{cases} \left[\frac{3}{2} \int_{\tau_t}^{\tau} \sqrt{|h(t)|} dt \right]^{2/3}, & \tau_t \le \tau, \\ -\left[\frac{3}{2} \int_{\tau}^{\tau_t} \sqrt{|h(t)|} dt \right]^{2/3}, & \tau \le \tau_t. \end{cases} \tag{21}$$

For the reference parameter values used for numerical calculations (as described in Sec. IV), $\delta \sim \nu^{-1}$ is around 1/300 to 1/150, so the WKBJ approximation is valid. Transitioning back to the model variables and functions, the radial mode function within the front can be approximated by

$$A_{Fn}(r) \sim a_0 F_1(r) + b_0 F_2(r), \tag{22}$$

where the linearly independent functions F_1 and F_2 are given by

$$F_1(r) = G(r)\mathrm{Ai}(\gamma g(r)), \quad F_2(r) = G(r)\mathrm{Bi}(\gamma g(r)), \tag{23}$$

with

$$G(r) = \sqrt{\frac{3}{2\gamma}} \left(\frac{g(r)}{z_r^2 - 1} \right)^{1/4}, \tag{24}$$

$$g(r) = \begin{cases} (\mu(z_r))^{2/3}, & r_t \le r, \\ -(\xi(z_r))^{2/3}, & r \le r_t, \end{cases} \tag{25}$$

$$\mu(z) = \sqrt{z^2 - 1} - \cos^{-1}\left(\frac{1}{z} \right), \tag{26}$$

$$\xi(z) = \ln\left(\frac{1 + \sqrt{1 - z^2}}{z} \right) - \sqrt{1 - z^2}, \tag{27}$$

and where $r_t = (q_F \delta)^{-1}$, $z_r = r/r_t$, and $\gamma = \left(\frac{3}{2}\sqrt{\nu^2 + (1/4)} \right)^{2/3}$.

Now that the radial mode functions have been approximated within the front, these approximations will be applied to the dispersion relation. For ease of calculation, the two

linearly independent functions $H_{-i\nu_n}^{(1)}(k_{rF}r)$ and $H_{-i\nu_n}^{(2)}(k_{rF}r)$ can be replaced in the dispersion relation given by Eq. (9) by the two approximated linearly independent functions F_1 and F_2. This will require the approximation of the quantities $F_1'(r)/F(r)$, $F_2'(r)/F(r)$, and $F_1(r)/F_2(r)$. After some lengthy calculations, the resulting approximations are

$$\frac{F_1'(r)}{F_1(r)} = \frac{1}{6r} \frac{\sqrt{z_r^2 - 1}}{g(r)^{3/2}} \left(1 + 4\gamma g(r) \frac{\mathrm{Ai}'(\gamma g(r))}{\mathrm{Ai}(\gamma g(r))} \right) - \frac{1}{2r} \frac{z_r^2}{z_r^2 - 1},$$

$$\frac{F_1(r)}{F_2(r)} = \frac{\mathrm{Ai}(\gamma g(r))}{\mathrm{Bi}(\gamma g(r))}, \tag{28}$$

and with $F_2'(r)/F_2(r)$ defined as $F_1'(r)/F_1(r)$ with $\mathrm{Ai}(\cdot)$ replaced with $\mathrm{Bi}(\cdot)$.

IV. INFLUENCE OF FRONT WIDTH VARIATIONN

Now consider numerical results for the following parameter values, which agree with those used by Lin and Lynch to allow for easier comparison:[6] center of the front at $r_I = 4000$ m, bottom slope $\alpha = 3°$, inshore sound speed $c_1 = 1500$ ms^{-1}, offshore sound speed $c_2 = 1520$ ms^{-1}, and source frequency $f = 25$ Hz. The values of the front width s will be given explicitly in the following numerical calculations. To determine the eigenvalues, the dispersion relation as given by Eq. (9) set equal to 1 is solved for k_y. The approach used to find these modes locates the curve in the complex k_y plane along which $|R_n| = 1$ within a thin strip, and then slices the strip into individual boxes containing intersections of $|R_n| = 1$ and contours of zero phase. The boxes containing eigenvalues are then iteratively refined to at most 10^{-8} in length along the real and imaginary axes, and the eigenvalue location within the refined box is approximated by calculating the intersection of the $|R_n| = 1$ and $\arg(R_n) = 0$ curves which are assumed to be nearly linear at this scale.

Figure 5(a) shows a portion of the k_y plane with eigenvalues for a 100 m front, and angular modes $n = 1$–3. Dashed vertical lines are placed to illustrate the separation between leaky modes and TR or WG modes, with leaky modes falling to the left of each color-coded dashed line (leaky/trapped division line for $n = 1$ is the right-most, while $n = 3$ is the left-most). Figures 5(b) and 5(c) give similar results for front widths of 50 and 0 m respectively.

A clear difference between the three illustrated front widths are the appearance and locations of local peaks in the imaginary components of k_y. These peaks occur at predictable values, when the differences in phase of the radial modes across the front are close to an integer multiple of π, achieving near-resonance. The phase difference across the front can be approximated by the front width multiplied by an average radial wavenumber in the front, leading to the simple equation

$$s\kappa_r(r_I) = N\pi, \tag{29}$$

for integers $N = 1, 2, 3, \ldots$, where any eigenvalues $k_{y,nm}$ for which Eq. (29) is approximately true can be classified as near resonant (NR). A simple relation between s and the k_y
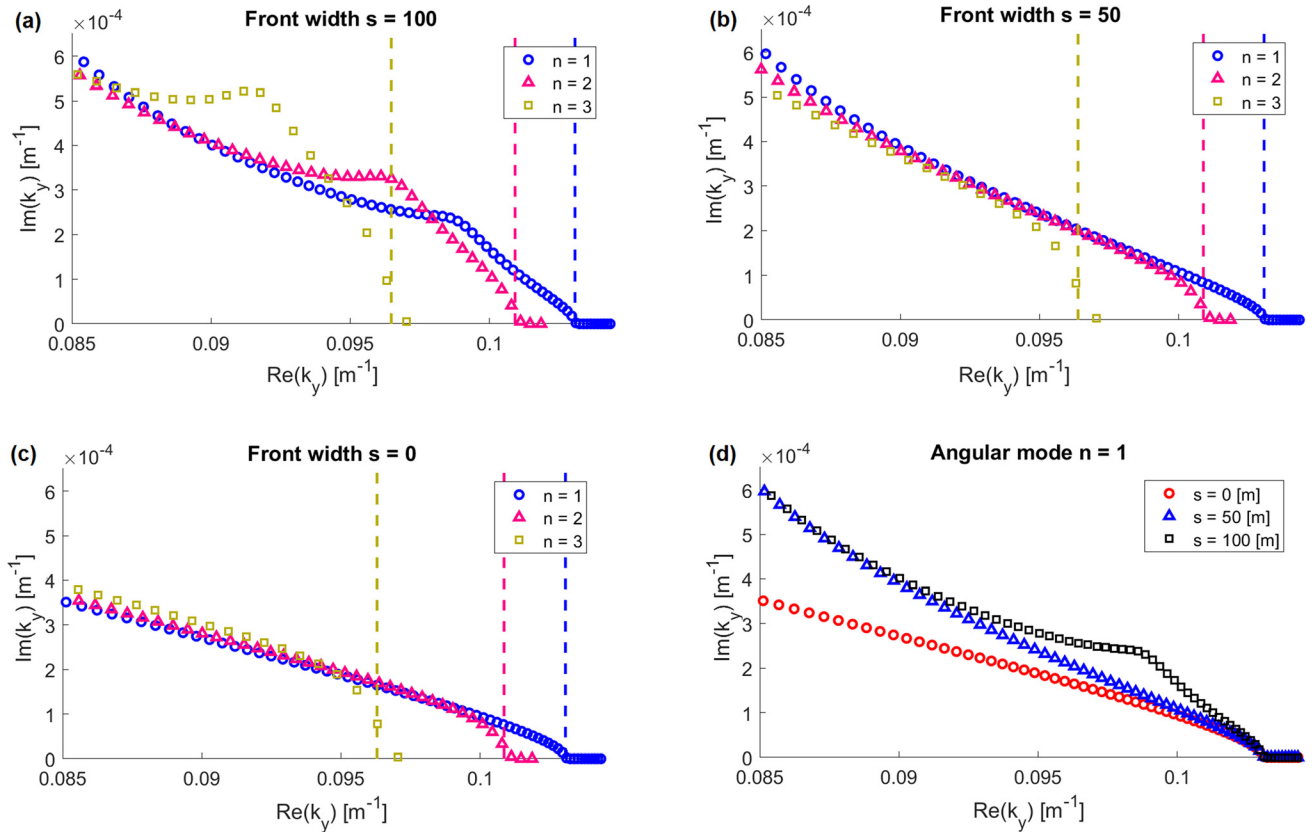
FIG. 5. (Color online) Radial mode eigenvalues in the k_y plane for angular mode numbers $n = 1$ (blue circles), $n = 2$, (red triangles), and $n = 3$ (brown squares). Vertical dashed lines represent $\mathrm{Re}(k_y)$ cut-off value separating leaky modes (to the left) from TR and WG modes (to the right). (a) Front width $s = 100$ m, (b) Front width $s = 50$ m, (c) Front width $s = 0$ m. (d) A comparison of angular modes $n = 1$ only for front widths $s = 0$ (red circles), $s = 50$ (blue triangles), $s = 100$ (black squares).

values for which near-resonance occurs can be achieved, by noting that for a fixed N in Eq. (29), s is inversely proportional to the radial wavenumber, such that an increase in s must be accompanied by a decrease in the real part of κ_r, which must in turn be accompanied by an increase in the real part of k_y by the relation $k^2(r) = \kappa_r^2(r) + k_y^2 + \eta_n^2/r^2$, assuming $\mathrm{Im}(k_y) \ll \mathrm{Re}(k_y)$. Therefore, as the front width increases, the first modes exhibiting near resonance occur at lower indices, and as s goes to zero near-resonance eventually disappears, agreeing with the behavior seen in Fig. 5.

One final difference to note is most clearly shown in Fig. 5(d), in which radial modes are plotted for $n = 1$ and the three front widths of 100, 50, and 0 m. A general trend of increasing $\mathrm{Im}(k_y)$ with increasing s is seen, which suggests that larger front widths are associated with "leakier" leaky modes, as higher energy decay along shore is necessarily related to higher transmission of energy offshore.

To see this last point more clearly, consider Fig. 6, which shows how individual modes change with front width. In both Figs. 6(a) and 6(b), all radial mode eigenvalues shown are associated with angular mode $n = 1$, and similar mode numbers m are connected by dashed lines across the various front widths of 0, 25, 50, 75, 100, and 200 m. The radial modes plotted are $m = 12$–21 in Fig. 6(a) and $m = 32$–41 in Fig. 6(b). Modes $m = 12$–21 are the lowest mode numbers associated with leaky modes at reference parameter values, with modes $m = 1$–11 being WG and TR

modes. For these leaky modes, the general trend observed is an increase in the imaginary component of k_y as the front width increases. It is also apparent that the growth of $\mathrm{Im}(k_y)$ with growing s is sensitive to the initial k_y value. In Fig. 6(b), a selection of modes that are near resonance are shown. Modes $m = 37$–41 do not exhibit a growth in $\mathrm{Im}(k_y)$ as s increases from 75 m, as the NR status of a mode disrupts the monotonic growth of $\mathrm{Im}(k_y)$ seen in modes 32–36, as well as all modes in Fig. 6(a).

Figure 7 illustrates the first five radial modes associated with each of the first three angular modes for a front width of $s = 100$ m, illustrated by the dashed horizontal lines. The trapping of energy that was seen by Lin and Lynch[6] is also present here, with the Whispering Gallery effect manifesting as a trapping of acoustic energy close to the inshore side of the interface. With this in mind, it is pertinent to address the effects of various front widths on the behavior of these WG and other modes to see if the physical simplification of an idealized front loses some of the expected behaviors, or if it is a strong representation of the acoustic ducting effects in this environment.

In Fig. 8, two radial modes are shown for angular mode $n = 1$ and front widths of $s = 0$, 100, and 200 m. For both modes pictured, the idealized front mode is given by the thick solid lines (blue for real components, red for imaginary), and the location of the idealized front is denoted by a thick vertical black line. For the front width of 100 m, the
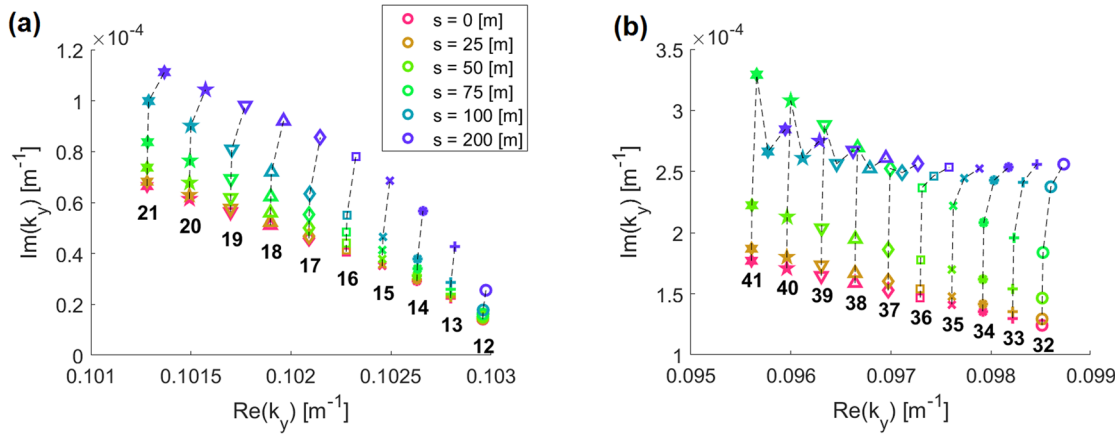
FIG. 6. (Color online) Evolution of eigenvalues in the k_y plane as front width changes. A single radial mode number m is represented by identical symbols connected by dashed lines. A collection of radial modes for a single front width s share the same color, corresponding to the legend. (a) Radial mode numbers $m = 12$ to 21, representing leaky modes with the lowest mode numbers. (b) Radial mode numbers $m = 32$ to 41, illustrating a non-monotonic growth of $\text{Im}(k_y)$ near NR modes.

modes are represented by thin solid lines, as are the inshore and offshore interfaces of the front, and the 200 m front is similarly represented by thin dashed lines. In Fig. 8(a), the WG mode $m = 8$ is shown, and for all front widths represented it appears to undergo very little perturbation, with the mode shapes for the three front widths sharing enough ink as to make the differences imperceptible in many areas. In contrast, Fig. 8(b) shows the leaky mode $m = 16$, and in this case the influence of front width is far more visible. Inshore, the mode shapes are in closer agreement for smaller r, with a slight phase shift appearing as the mode approaches the

front, as well as a slight growth in mode amplitude. Offshore, the phase and amplitude differences are more exaggerated, with amplitude nearly doubling a short distance front the front. Figure 8(c) shows a closer view of the front region for $m = 16$, in which it is clear that the divergence from the idealized mode shape is far more exaggerated for the front width of 200 m compared with 100 m. The behaviors seen in these two modes in Fig. 8 are not too surprising, as the eigenvalue behavior shown in Figs. 5 and 6 suggest that $\text{Im}(k_y)$ increases with increasing front width, and that this increase is greater for larger radial mode numbers, i.e.,
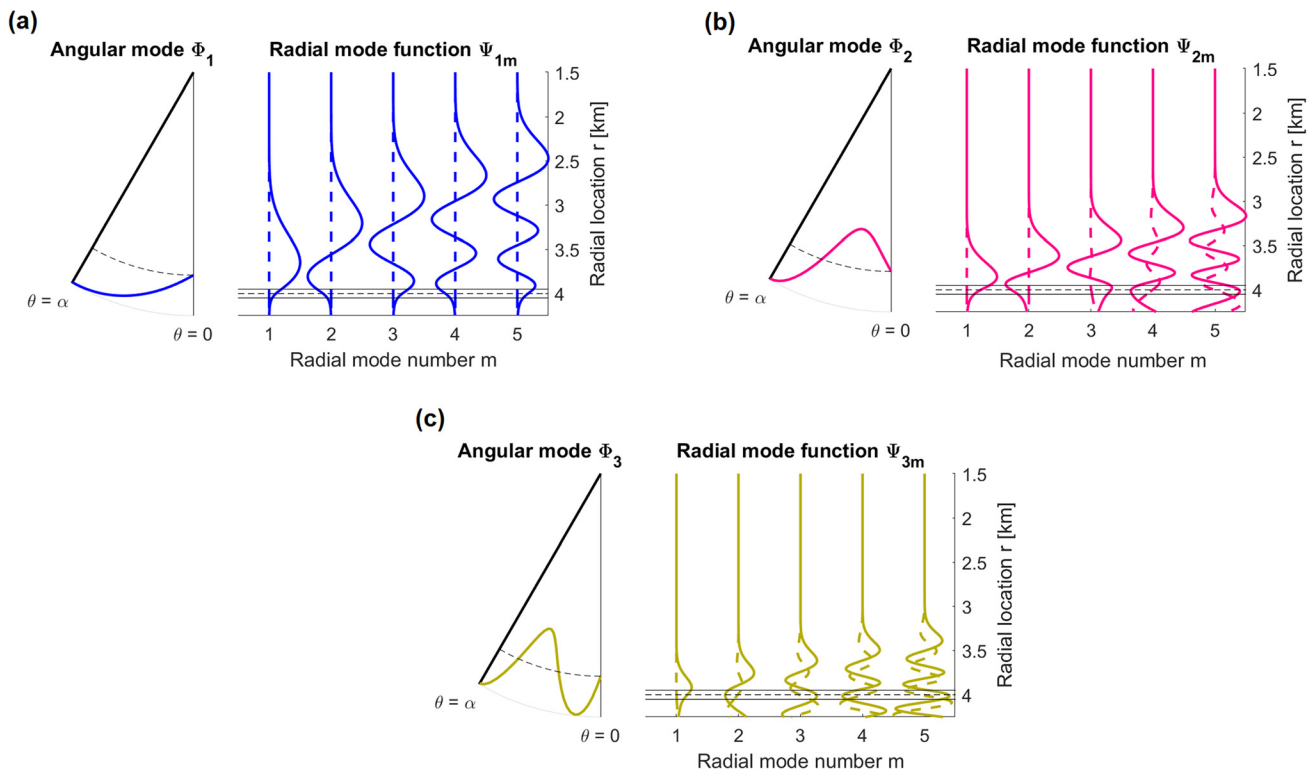

FIG. 7. (Color online) Sample radial and angular mode profiles for front width of 100 m: (a) Angular mode $n = 1$ and radial modes $m = 1$–5, (b) angular mode $n = 2$ and radial modes $m = 1$–5, (c) angular mode $n = 3$ and radial modes $m = 1$–5. Real components shown as solid lines, imaginary components as dashed lines.

J. Acoust. Soc. Am. **146** (3), September 2019
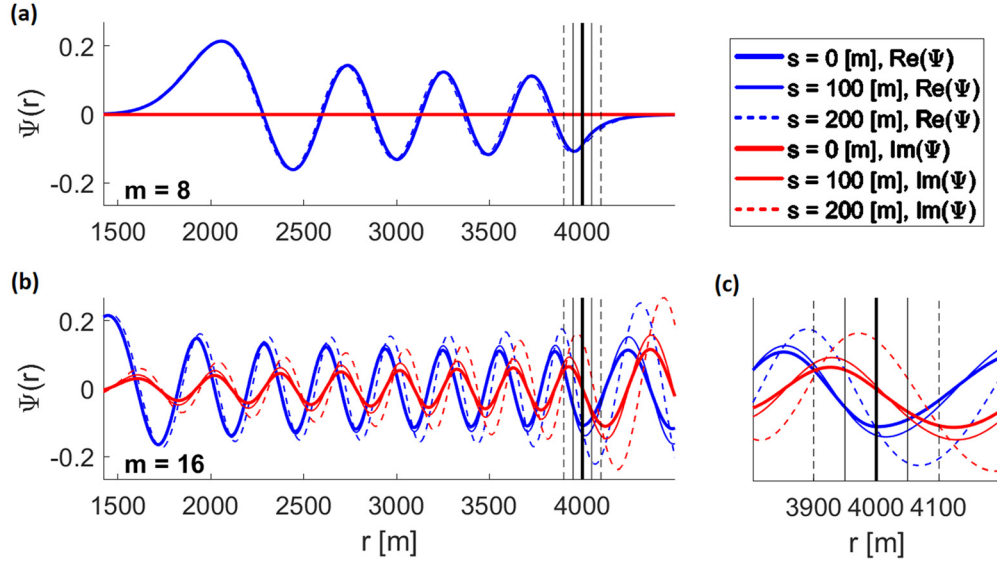
DeCourcy *et al.* 1929

FIG. 8. (Color online) Illustration of the evolution of radial mode shape as front width changes. Blue (dark) lines represent real components, while red (light) represent imaginary components. The thick solid lines represent a reference idealized front with $s = 0$ m, thin solid lines represent a front width of $s = 100$ m, and dashed lines represent a front width of $s = 200$ m. Vertical thick solid, thin solid, and dashed lines represent the idealized, 100 m, and 200 m fronts, respectively. (a) Mode $n = 1$, $m = 8$, (b) mode $n = 1$, $m = 16$, (c) close-up on the front region of $n = 1$, $m = 16$.

"leakier" modes. An interpretation of these results is that the trapping behavior exhibited by WG and TR modes which have zero or nearly zero $\text{Im}(k_{y,nm})$ is captured well by the idealized front model, while the leaky modes are not.

The goal of the approximation of Eq. (15) which ignores contributions from branch line integrals is to conveniently represent the far-field behavior in y. It is expected that by excluding the branch line integrals, the near-field will lose accuracy, but by including leaky modes that are exposed by the Pekeris branch cut, an approximation of the near-field can be achieved.[18] The far-field is described by the WG and TR modes, which propagate long distances along shore in the y direction due to their zero or near-zero $\text{Im}(k_{y,nm})$ values, while leaky modes will have little influence in the far-field due to their larger $\text{Im}(k_{y,nm})$ values. Closer to the source, more leaky modes are required to represent the field, and with larger front widths associated with higher $\text{Im}(k_y)$ values in the leaky modes, the influence of leaky modes will be less apparent in the far-field for larger width continuous fronts. A rough approximation of the limit on the influence of a single leaky mode can be calculated by assuming that behavior of a single mode in the (r, y) plane is largely governed by the plane wave approximation $\exp(i\kappa_{r,nm}(r)r + ik_{y,nm}y)$. Using a $1/e$ decay rate to judge the influence of leaky modes in the (r, y) plane, the range in y that a leaky mode will propagate at a given r and for a given eigenvalues $k_{y,nm}$ is approximately $y = \tilde{y}(r; n, m) = [1 - \text{Im}(\kappa_{r,nm}(r))r]/\text{Im}(k_{y,nm})$, where $\kappa_{r,nm}(r) = \sqrt{k^2(r) - k_{y,nm}^2 - (\eta_n^2/r^2)}$. To properly evaluate the acoustic pressure at a location (r^*, y^*), all modes for which $\tilde{y}(r^*; n, m) > y^*$ must be included. This leads naturally to the definition

$$y_{max}(r; n) = \tilde{y}(r; n, M), \tag{30}$$

where M is the last in a finite set of consecutive mode numbers beginning with 1.

Figure 9 gives the transmission loss field in the (r, y) plane located at $\theta = 1.5°$ for a source located at $(r_0, \theta_0, y_0) = (3900 \text{ m}, 1.5°, 0 \text{ m})$, and with a front width of $s = 100$ m. Figures 9(a)–9(c) show the contributions from angular modes $n = 1$, 2, and 3 respectively, with 66 radial modes in Fig. 9(a), 42 modes in Fig. 9(b), and 24 modes in Fig. 9(c) to illustrate the extent that a finite sum of modes can represent the far-field. Figure 9(d) includes all modes represented in Figs. 9(a)–9(c). In all subfigures, the dotted lines represent the y_{max} value which denotes the limit to the accuracy of a finite sum approximation under the $1/e$ decay condition. Regions of the (r, y) plane to the right of and above these lines are well represented by the finite sum of modes, as all modes that propagate into that region are included, while the regions to the left of and below these lines cannot be considered accurately represented, as not all modes that contribute to that portion of the field are included. In Fig. 9, only the positive y axis is shown as the field is symmetric across $y = 0$.

To best understand the impact of front representation on the acoustic ducting effect, a relative difference between the transmission loss in a 100 m front model compared to an 0 m front model can be considered, by examining $\mathcal{D}_{100} = |TL_0 - TL_{100}|/TL_0$, where TL_s is the transmission loss calculated for a front of width s. Figure 10(a) illustrates this value in the (r, y) plane at $\theta_0 = 1.5°$ and $r_0 = 3900$ m, using the same m and n values present in Fig. 9 for the front of 100 m, and analogous mode numbers for the idealized front of 0 m. Four relative difference levels are considered: $\mathcal{D}_{100} < 0.01$, $\mathcal{D}_{100} < 0.05$, $\mathcal{D}_{100} < 0.1$, and $\mathcal{D}_{100} > 0.1$, with higher relative difference represented by darker shades. Additionally, the relative field differences are shown for a source located at $r = 3900$ m (a) and a source at $r = 3000$ m (b) to illustrate the effects of the front representation for a source located farther inshore, and that the influence of the sharp front approximation is less pronounced for such a source location.
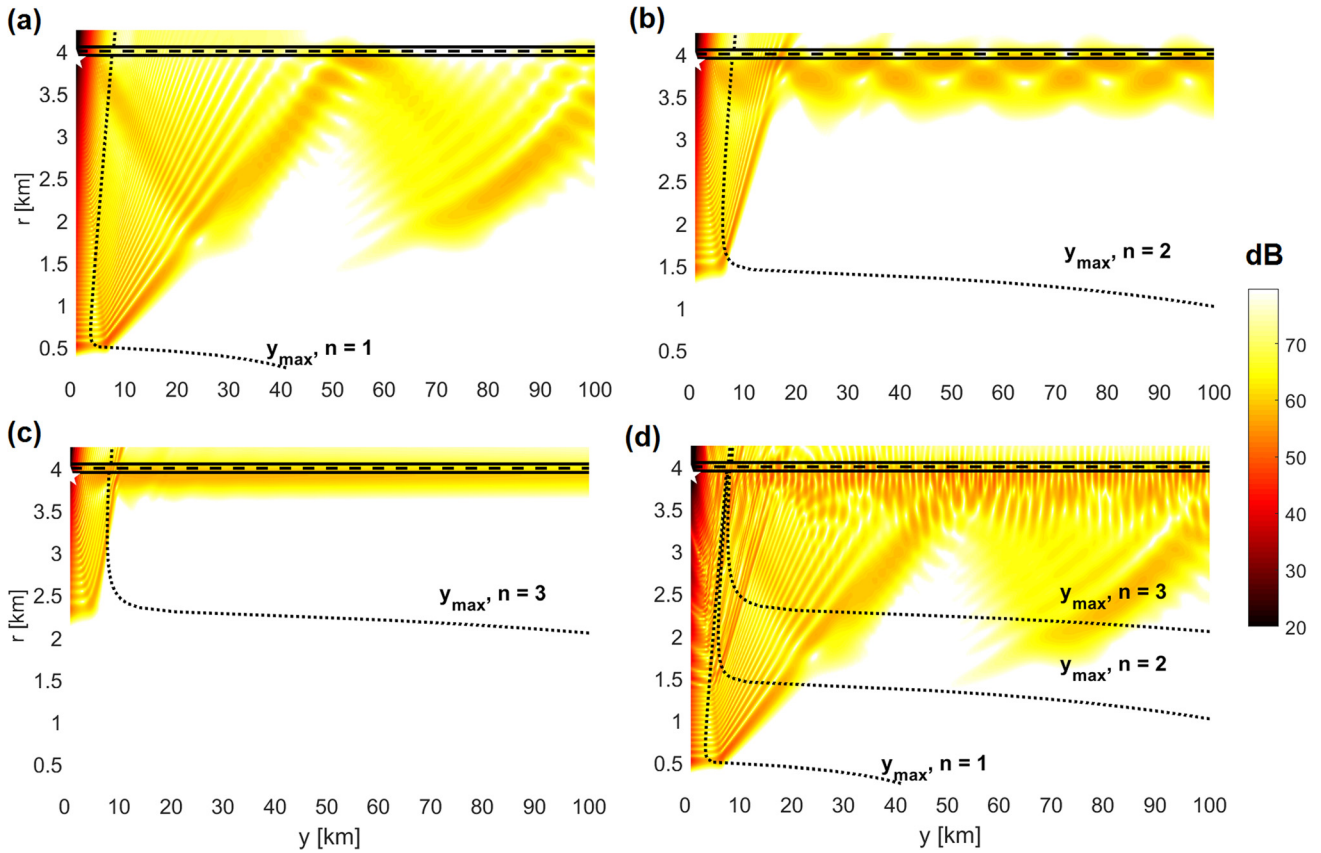
DeCourcy *et al.*

FIG. 9. (Color online) Transmission loss fields in the (r, y) plane at $\theta = 1.5°$, for a source located at $r_0 = 3900\,m$, $y_0 = 0\,m$, $\theta_0 = 1.5°$ denoted by a white star, and a front width of $s = 100\,m$. (a) Contribution from angular mode $n = 1$ and radial modes $m = 1–66$. Horizontal solid lines represent the front interfaces, while the horizontal dashed line is at $r = r_I$. The dotted curves represent the locations of e^{-1} decay for modes at the given n. (b) Angular mode $n = 2$, radial modes $m = 1–42$. (c) Angular mode $n = 3$, radial modes $m = 1–24$. (d) All modes from (a)–(c).

First, consider the regions in Fig. 10(a) which indicate agreement between the two fields within 1%, shown in white in the contour plot. These areas are concentrated largely where the ducting is observed, between the front and the inshore shadow zones. The introduction of the 100 m continuous front does little to alter this behavior inshore, which is dominated by the WG and TR modes. This is expected, as it was previously observed that the WG and TR modes are not as sensitive to the front width compared to leaky modes.
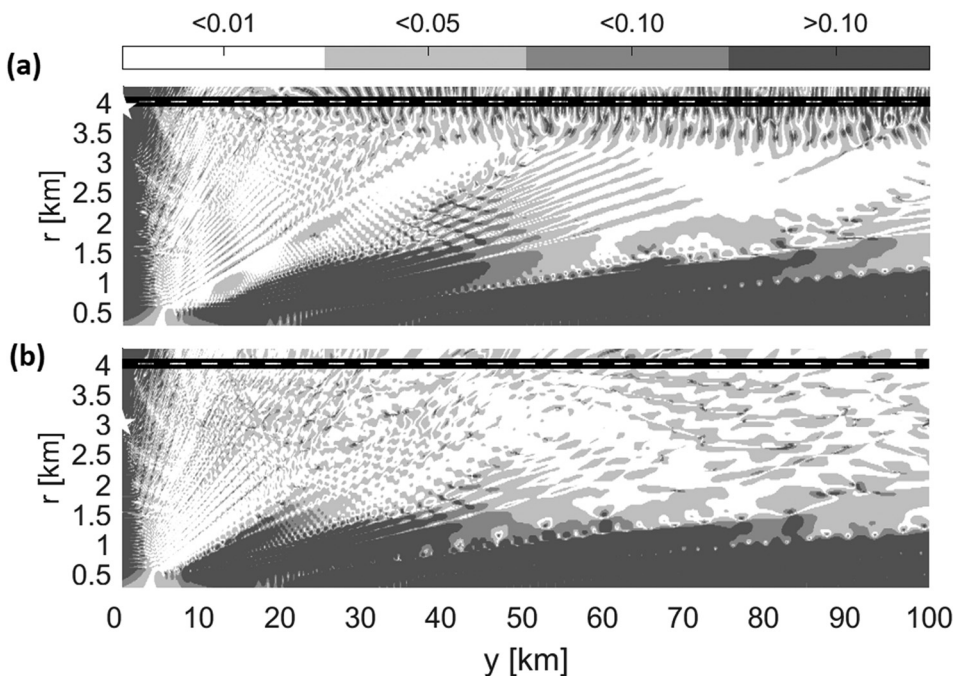

FIG. 10. Relative difference $\mathcal{D}_{100} = |TL_0 - TL_{100}|/TL_0$ between transmission loss fields for front widths of 0 and 100 m. The four color levels represent agreement to within 1%, 5%, 10%, or greater than 10% in order of increasing shades.

In the darkest shaded regions of Fig. 10(a), the relative difference between the two considered TL fields is greater than 10%. Three major regions of disagreement are observed: the near field, close to $y = 0$, the shadow zones close to $r = 0$, and the front region, close to $r = r_I$. For the near-field, disagreement between the 100 and 0 m fronts is not of significant interest, as the approximation given here is for the far-field, and not enough leaky modes are included to arrive at any conclusions for this area. In the shadow zones inshore, energy does not propagate, so disagreement between the two fields is also of little interest, as much of it could be due to limits in numerical accuracy for small values. The primary region of interest for disagreement between the two fields is in the vicinity of the front. It is clear that the interference patterns for the two front widths do not align, so this must be considered when choosing to use an idealized front model to gain insight on interference patterns near the front, and this becomes more important when the source is close to the front.

V. CONCLUSION

The effects on acoustic propagation of a curved continuously varying sound speed front over a sloping bottom are examined in comparison to a benchmark model of an idealized front by Lin and Lynch.[6] To account for the continuous front, an inverse square wavenumber profile is used in place of a sharp discontinuity, which has the benefit of convenient mathematical interpretations in terms of Hankel functions. With the introduction of a more physically acceptable front representation, the same mode types that appeared in the idealized model are present, with the whispering gallery modes that account for trapping of energy on the inshore side of the front exhibiting nearly identical mode shapes for those front widths considered when comparing with the idealized results. In contrast, leaky modes behave quite differently than their idealized counterparts, propagating shorter distances along shore as more energy passes through the front rather than being refracted by it. In addition to the difference in the amount of ducted energy for the leaky modes, some leaky modes can be classified as near-resonant in the continuous model, which can be characterized by a larger imaginary component in the associated k_y eigenvalue, indicating stronger transmission across the front than neighboring modes.

Despite the noted differences, the idealized front model does an excellent job of describing the general acoustic ducting behavior inshore. Notable deviations from the continuous model are exhibited mainly in the interference patterns near the front, due to the reflective nature of the idealized model compared with the refractive nature of a continuous sound speed front. For the purposes of providing insight into the shelf-slope environment, representing the front with an idealized jump in sound speed does not significantly alter the along-front ducting of sound inshore, such that interest in inshore propagation in the shelf-slope front environment can be safely investigated with the convenient idealized front formulation. The structure of the front will understandably play a larger role in behavior in and around the front, in which case it is recommended that a continuous representation is considered.

[1]T. H. Kinder and L. K. Coachman, "The front overlaying the continental slope in the Eastern Bering Sea," J. Geo. Res. **83**, 4551–4559 (1978).

[2]A. R. Parsons, R. H. Bourke, R. D. Muench, C.-S. Chiu, J. F. Lynch, J. H. Miller, A. J. Plueddemann, and R. Pawlowicz, "The Barents Sea Polar Front in summer," J. Geo. Res. **101**, 14201–14221 (1996).

[3]C. A. Linder and G. Gawarkiewicz, "A climatology of the shelfbreak front in the Middle Atlantic Bight," J. Geo. Res. **103**, 18405–18423 (1998).

[4]J. F. Lynch, A. E. Newhall, B. Sperry, G. Gawarkiewicz, A. Fredricks, P. Tyack, C.-S. Chiu, and P. Abbot, "Spatial and temporal variations in acoustic propagation characteristics at the New England Shelfbreak Front," IEEE J. Ocean. Eng. **28**, 129–149 (2003).

[5]B. J. Sperry, J. F. Lynch, G. Gawarkiewicz, C.-S. Chiu, and A. Newhall, "Characteristics of acoustic propagation to the Eastern Vertical Line Array Receiver during the Summer 1996 New England Shelfbreak PRIMER Experiment," IEEE J. Ocean. Eng. **28**, 729–749 (2003).

[6]Y.-T. Lin and J. F. Lynch, "Analytical study of the horizontal ducting of sound by an oceanic front over a slope," J. Acoust. Soc. Am. **131**, EL1–EL7 (2012).

[7]B. J. DeCourcy, Y.-T. Lin, and W. L. Siegmann, "Approximate formulas and physical interpretations for horizontal acoustic modes in a shelf-slope front model," J. Acoust. Soc. Am. **140**, EL20–EL25 (2016).

[8]B. J. DeCourcy, Y.-T. Lin, and W. L. Siegmann, "Estimating the parameter sensitivity of acoustic mode quantities for an idealized shelf-slope front," J. Acoust. Soc. Am. **143**, 706–715 (2018).

[9]M. J. Buckingham, "On acoustic transmission in ocean-surface waveguides," Philos. Trans. Phys. Sci. Eng. **335**, 513–555 (1991).

[10]A. J. Robins, "Reflection of a plane wave from a fluid layer with continuously varying density and sound speed," J. Acoust. Soc. Am. **89**, 1686–1696 (1991).

[11]F. B. Jensen and W. A. Kuperman, "Sound propagation in a wedge-shaped ocean with a penetrable bottom," J. Acoust. Soc. Am. **67**, 1564–1566 (1980).

[12]G. B. Deane and C. T. Tindle, "A three-dimensional analysis of acoustic propagation in a penetrable wedge slice," J. Acoust. Soc. Am. **92**, 1583–1592 (1992).

[13]G. B. Deane and M. J. Buckingham, "An analysis of the three-dimensional sound field in a penetrable wedge with a stratified fluid or elastic bottom," J. Acoust. Soc. Am. **93**, 1319–1328 (1993).

[14]A. D. Heathershaw, C. E. Stretch, and S. J. Maskell, "Coupled ocean-acoustic model studies of sound propagation through a front," J. Acoust. Soc. Am. **89**, 145–155 (1991).

[15]G. V. Frisk, *Ocean and Seabed Acoustics: A Theory of Wave Propagation* (Prentice-Hall, Englewood Cliffs, NJ, 1994), Chap. 4.7, Appendix B.

[16]A. D. Pierce, "Extension of the method of normal modes to sound propagation in an almost-stratified medium," J. Acoust. Soc. Am. **37**, 19–27 (1965).

[17]C. M. Bender and S. A. Orszag, *Advanced Mathematical Methods for Scientists and Engineers* (McGraw-Hill, New York, 1978), Chap. 1.5.

[18]F. B. Jensen, W. A. Kuperman, M. B. Porter, and H. Schmidt, *Computational Ocean Acoustics*, 2nd ed. (Springer, New York, 2011), Chap. 1, Sec. 1.3.4; Chap. 2, Secs. 4.5.2, 4.6.2.

[19]D. C. Stickler, "Normal-mode program with both the discrete and branch line contributions," J. Acoust. Soc. Am. **57**, 856–861 (1975).

[20]M. J. Ablowitz and A. S. Fokas, *Complex Variables: Introduction and Applications*, 2nd ed. (Cambridge University Press, New York, 2003), pp. 206–207.

[21]M. Abramowitz and I. A. Stegun, *Handbook of Mathematical Functions* (Dover Publications, New York, 1964), p. 358.

[22]R. B. Evans, "The existence of generalized eigenfunctions and multiple eigenvalues in underwater acoustics," J. Acoust. Soc. Am. **92**, 2024–2029 (1992).

[23]W. E. Zorumski and J. P. Mason, "Multiple eigenvalues of sound-absorbing circular and annular ducts," J. Acoust. Soc. Am. **55**, 1158–1165 (1974).

[24]M. H. Holmes, *Introduction to Perturbation Methods*, 2nd ed. (Springer, New York, 2013), Sec. 4.3.